


# Molecular Insights into the Microscopic Behavior of CO<sub>2</sub> Hydrates in Oceanic Sediments: Implications for Carbon Sequestration

Fengyi Mi, Wei Li, Jiangtao Pang, Othonas A. Moulτος, Fulong Ning,\* and Thijs J.H. Vlught\*

 Cite This: *J. Phys. Chem. C* 2024, 128, 18588–18597

 Read Online

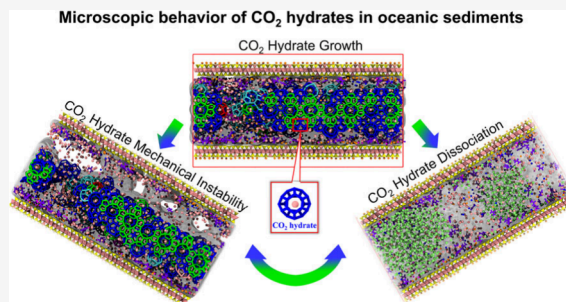
ACCESS |

 Metrics & More

 Article Recommendations

 Supporting Information

**ABSTRACT:** Knowledge of the microscopic behavior of CO<sub>2</sub> hydrates in oceanic sediments is crucial to evaluate the efficiency and stability of hydrate-based CO<sub>2</sub> sequestration in oceans. Here, systematic molecular dynamics simulations are executed to investigate the growth and dissociation of CO<sub>2</sub> hydrates, and the mechanical instability of CO<sub>2</sub> hydrate-Illite interface in the brine-urea-Illite system. Simulation results show that the CO<sub>2</sub> hydrate growth is jointly affected by the confined space, Illite surface properties, and presence of urea. Specifically, the interfacial H<sub>2</sub>O and the ion layer on the Illite surface hinder the growth of CO<sub>2</sub> hydrate crystals toward Illite surfaces. Urea molecules can bind salt ions and increase CO<sub>2</sub> concentrations in the water, thus kinetically promoting CO<sub>2</sub> hydrate growth. The dissociation of the CO<sub>2</sub> hydrate is affected by Illite surface properties and the CO<sub>2</sub> hydrate structure. CO<sub>2</sub> hydrate starts from the regions where hydrate particles are minimally in contact and extends on both sides. The mechanical tension and compression of the CO<sub>2</sub> hydrate-Illite interface exhibit nonlinear characteristics by changing the hydrogen bonds and the CO<sub>2</sub> hydrate structure. The molecular insight into the microscopic behavior of CO<sub>2</sub> hydrates in the brine-urea-Illite system contributes to a broader understanding of hydrate-based CO<sub>2</sub> sequestration.



## 1. INTRODUCTION

Decarbonization emerges as a critical issue for the forthcoming decades. CO<sub>2</sub> gas produced by humans is one of the main greenhouse gases and worsens global warming. A prospective method involves the injection of CO<sub>2</sub> into seafloor sediments, where it undergoes a transformative process, manifesting as CO<sub>2</sub> hydrate.<sup>1–3</sup> CO<sub>2</sub> hydrates are nonstoichiometric crystalline compounds wherein CO<sub>2</sub> molecules are bound within a cage-like network formed by water molecules via hydrogen bonds.<sup>4</sup> The seafloor environment, characterized by low temperatures and high pressures, facilitates the rapid formation of CO<sub>2</sub> hydrates. Evidence from field tests highlights the efficacy of liquid CO<sub>2</sub> injection into seafloor depths ranging from 2700 to 4500 m, resulting in the rapid reaction with water and the formation of CO<sub>2</sub> hydrates.<sup>5</sup> The stable storage of natural gas hydrates in seafloor sediments for millennia is well-documented.<sup>6,7</sup> The complex nature of sedimentary environments such as solid surfaces, salt ions, and organic matter, complicate the formation and growth processes of CO<sub>2</sub> hydrates in marine sediments.<sup>8,9</sup> A comprehension of the microscopic mechanisms of CO<sub>2</sub> hydrates in complex seafloor sediments is imperative for advancing hydrate-based CO<sub>2</sub> sequestration.

The formation kinetics and sequestration stability of CO<sub>2</sub> hydrates are significantly influenced by various marine environmental factors.<sup>9</sup> Clay minerals, a major constituent of seafloor sediments, exert a crucial role in regulating both hydrate formation and decomposition processes.<sup>10–16</sup> Exper-

imental results indicated that clay minerals can serve as hydrate nucleation sites to significantly shorten the induction time and promote hydrate formation.<sup>17–22</sup> Recent investigations by Ren et al. indicate that swelling montmorillonite clay enhances hydrate nucleation while concurrently retarding the growth kinetics of gas hydrates.<sup>23–25</sup> The salt ions in the ocean inevitably affect the thermodynamics and dynamics of the hydrates. Conventionally viewed as hydrate inhibitors due to their impact on the water molecule activity, recent studies reveal that specific inorganic salts and low salinity can also promote hydrate formation by controlling the distribution of surrounding H<sub>2</sub>O and guest molecules.<sup>26–30</sup> Molecular dynamics (MD) simulations emerge as valuable tools for unraveling the microscopic behavior of gas hydrates, showcasing insights unattainable through experiments.<sup>31–38</sup> Our prior MD simulation reported that the interaction of salt ions with the clay surface can change the local concentration of guest molecules and the location of hydrate formation.<sup>39–41</sup>

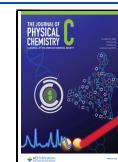
The vast ocean, serving as a reservoir of organic matter, introduces additional layers of complexity to the efficiency and

**Received:** August 12, 2024

**Revised:** October 4, 2024

**Accepted:** October 10, 2024

**Published:** October 21, 2024



stability of CO<sub>2</sub> hydrate sequestration in seafloor sediments.<sup>8,42,43</sup> Several experimental and simulation results suggested that organic matter molecules inhibit the phase equilibrium and formation kinetics of hydrates by binding to water molecules.<sup>44–49</sup> Kyung et al. found that the interfacial interactions between organic matter and clay surfaces promote CO<sub>2</sub> hydrate formation kinetics.<sup>50</sup> Zhao et al. reported a 92% reduction in the induction time of CO<sub>2</sub> hydrates from organoclay solution.<sup>9</sup> Urea, as a low-toxic biological metabolite, exhibits a dual influence on CO<sub>2</sub> hydrate formation, i.e., acting both as a thermodynamic inhibitor and a kinetic promotor.<sup>51–56</sup> Urea can greatly shorten the induction time and promote hydrate formation.<sup>57–59</sup> The interactions of urea, ions, and clay minerals in the ocean complicate the growth and dissociation of CO<sub>2</sub> hydrates in seafloor sediments. Considering the significance of hydrate stability in evaluating hydrate-based CO<sub>2</sub> sequestration, concerns arise about the long-term stability and potential environmental hazards, such as submarine landslides, CO<sub>2</sub> leaks.<sup>60–62</sup> Therefore, it is necessary to understand the effect of complex marine environments on the growth and stability of CO<sub>2</sub> hydrates in marine sediments. From a physicochemical perspective, the formation of CO<sub>2</sub> hydrates involves complex molecular interactions, including guest CO<sub>2</sub> and water molecules. The interactions with the Illite surface and the presence of ions such as Na<sup>+</sup> and Cl<sup>−</sup> introduce additional complexity, which are fundamental to understanding both the thermodynamics and kinetics of hydrate formation and dissociation.<sup>63–65</sup>

In this study, systematic MD simulations were executed to investigate the growth and dissociation of CO<sub>2</sub> hydrates, and the mechanical instability of the CO<sub>2</sub> hydrate-Illite interface in the brine-urea-Illite system. The microscopic behavior of CO<sub>2</sub> hydrates in oceanic sediments was revealed, contributing valuable insights into the broader understanding of hydrate-based CO<sub>2</sub> sequestration. We feel that this preliminary investigation is poised to catalyze further original research, particularly in uncovering novel CO<sub>2</sub> hydrate promoters and identifying potential marine CO<sub>2</sub> sequestration sites.

## 2. SIMULATION MODELS AND METHODS

An Illite layer is created by replicating the unit cell (24 × 8 × 1) with the chemical formula K<sub>1</sub>(Si<sub>7</sub>Al)Al<sub>4</sub>O<sub>20</sub>(OH)<sub>4</sub>. An Illite nanopore consists of two identical Illite layers, and the size of the Illite nanopore was determined to be 46 Å. Previous studies revealed that a too-small nanopore is not conducive to hydrate formation.<sup>66</sup> A CO<sub>2</sub> hydrate crystal (2 × 6 × 4) and a homogeneous solution (containing CO<sub>2</sub>, H<sub>2</sub>O, Na<sup>+</sup>, Cl<sup>−</sup> and K<sup>+</sup>) were inserted into the Illite nanopore. Various numbers of urea were introduced into the Illite nanopores to represent different urea concentrations (1.6%, 3%, 4.5%, and 6%), as shown in Table 1. This allows a precise analysis of the

**Table 1. Parameters for Each System of CO<sub>2</sub> Hydrate in Oceanic Sediments**

system	growth + dissociation + instability		
	$N_{\text{urea}}$	urea concentration	simulation time
H <sub>0%</sub> Urea	0	0 wt %	2 μs + 10 ns + 1 ns
H <sub>1.6%</sub> Urea	64	1.6 wt %	2 μs + 10 ns + 1 ns
H <sub>3%</sub> Urea	127	3 wt %	2 μs + 10 ns + 1 ns
H <sub>4.5%</sub> Urea	191	4.5 wt %	2 μs + 10 ns + 1 ns
H <sub>6%</sub> Urea	254	6 wt %	2 μs + 10 ns + 1 ns

interaction between urea and geofluid, which has been frequently employed in previous simulations and experiments.<sup>52,56</sup> A system without urea molecules was simulated as a reference. The urea concentrations provided in Table 1 refer to the initial concentration based on the number of urea molecules introduced at the beginning of the simulation. Five simulation systems containing homogeneous solutions and CO<sub>2</sub> hydrate crystals with different urea concentrations were executed, namely H<sub>0%</sub>Urea, H<sub>1.6%</sub>Urea, H<sub>3%</sub>Urea, H<sub>4.5%</sub>Urea, and H<sub>6%</sub>Urea. The parameters of each simulation are listed in Table S1 and Table S2. Additionally, two layers of virtual walls were added to the box in the z-direction to avoid periodic interactions between the clay layers. Details of the method and parameters for virtual walls were provided in the Supporting Information. The dissociation of the CO<sub>2</sub> hydrate was simulated by increasing the temperature to 307 K.<sup>67</sup>

CO<sub>2</sub> molecules, H<sub>2</sub>O molecules, Illite, and urea molecules are described by the TraPPE,<sup>68</sup> the TIP4P/Ice,<sup>69</sup> the CLAYFF,<sup>70</sup> and the OPLS-AA force field,<sup>71</sup> respectively. All growth simulations were performed using the molecular dynamics GROMACS package (version 2022)<sup>72</sup> in the isothermal–isobaric *NPT* ensemble at a fixed pressure of 500 bar and temperature of 250 K. The system was equilibrated with a Nosé–Hoover<sup>73</sup> thermostat and a Parrinello–Rahman<sup>74</sup> barostat with time constants of 1 and 4 ps, respectively. The pressure coupling utilized a semi-isotropic barostat, and the pressure scaling only works in the z direction. The cutoff radius for computing the van der Waals forces was set to 10 Å. For electrostatic energy computation, the particle-mesh Ewald<sup>75</sup> algorithm was used with the cutoff as 10 Å and Fourier grid spacing of 1.2 Å. The periodic boundary conditions were applied in *xy* directions, and the *z* direction was restricted by the virtual wall (Figure 1).

## 3. RESULTS AND DISCUSSION

**3.1. The Interface Behavior between Geofluid and Illite Clay during CO<sub>2</sub> Hydrate Growth.** Understanding the interface behavior between geofluids (e.g., H<sub>2</sub>O, CO<sub>2</sub>, ions, and urea) and clay surfaces is of great significance to hydrate-based CO<sub>2</sub> sequestration. During the growth process of the CO<sub>2</sub> hydrates, the Illite surface exhibits different affinities toward geofluids. The density curves of geofluids are illustrated in Figure 2(a) and S1(a–e). It is found that CO<sub>2</sub>, ions, H<sub>2</sub>O, and urea molecules all form the interfacial layer on the Illite surface (Figure 2(a) and S1(a–e)). Specifically, cations swiftly adsorb on the Illite surface in a short time to compensate for the negative charge of the Illite surface. The number of ions in the Illite interface region first increases rapidly and then slowly increases (Figure 2(b) and S2(a–e)). Most of the ions are distributed in the Illite interface region (Figure S3(a–e)). Although CO<sub>2</sub> molecules form an interfacial layer on the Illite surface (Figure 2(a) and S1(a–e)), the number of CO<sub>2</sub> molecules within the Illite interface region decreases gradually (Figure 2(b) and S2(a–e)). This may be due to the adsorption of H<sub>2</sub>O, ions, and urea molecules on the Illite surfaces, which hinders the adsorption of CO<sub>2</sub> molecules. As CO<sub>2</sub> hydrate grows, CO<sub>2</sub> hydrate solids gradually extend toward the Illite interface region (Figure S4(a–e)), consequently increasing the number of CO<sub>2</sub> molecules therein (Figure 2(b) and S2(a–e)). The Illite surface can adsorb H<sub>2</sub>O molecules due to the hydrogen bonds between the abundant siloxanes on the Illite surface and H<sub>2</sub>O molecules (Figure 2(c) and S5(a–e)). The hydrogen bonds formed by H<sub>2</sub>O molecules and Illite surfaces

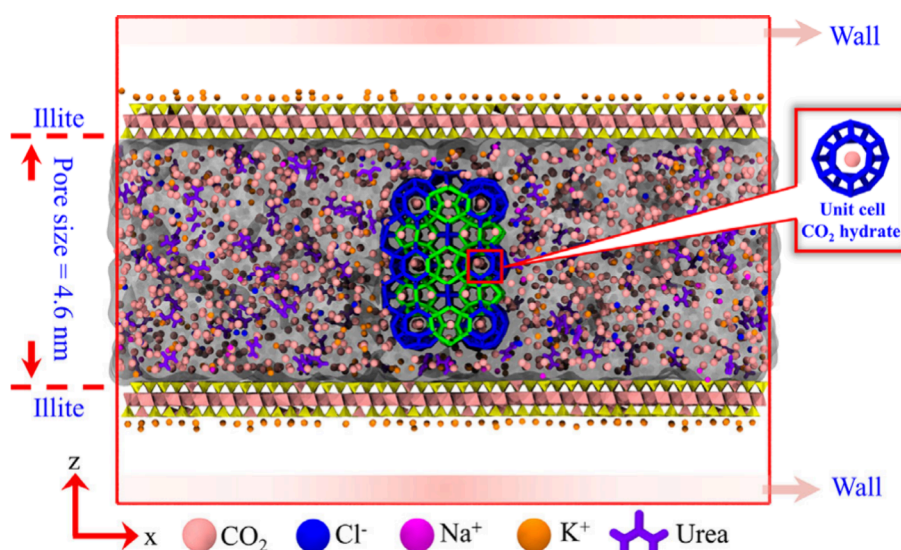


**Figure 1.** A schematic representation of the initial simulation model. Illite is displayed as polyhedral, i.e., yellow (Si atom), and pink (Al atom). Pink, blue, magenta, orange, and violet represent CO<sub>2</sub>, Cl<sup>-</sup>, Na<sup>+</sup>, K<sup>+</sup>, and urea, respectively.

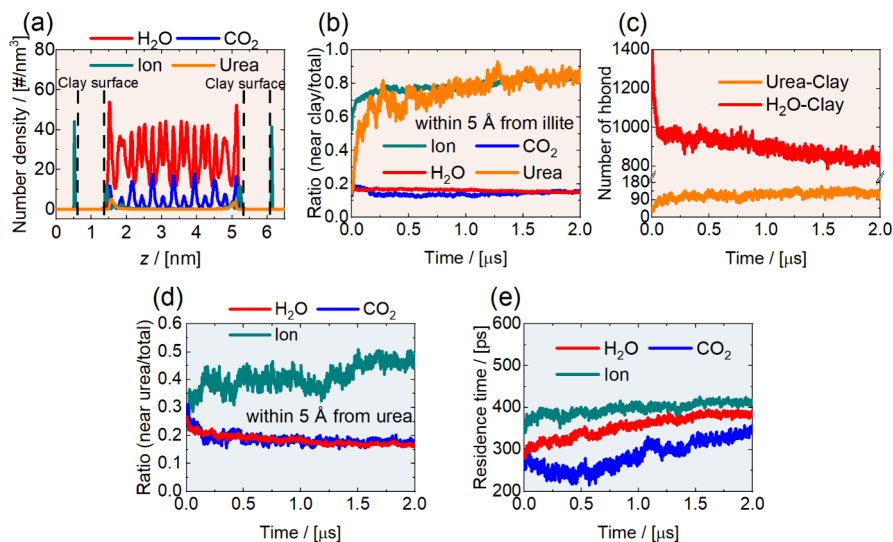


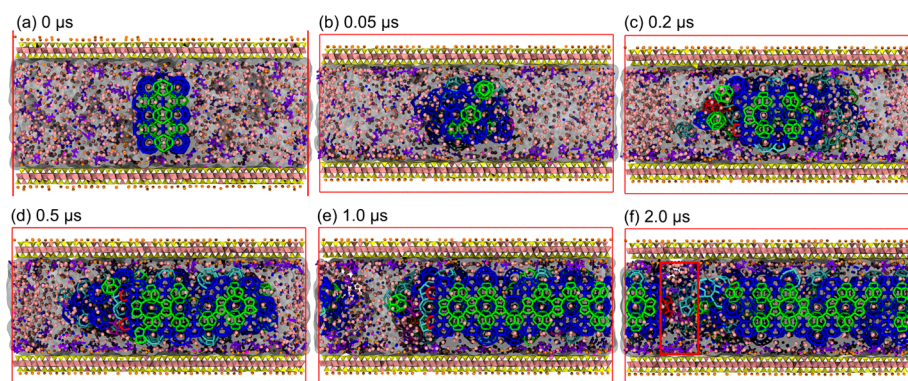
**Figure 2.** (a) Density distribution curves of geofluids (H<sub>2</sub>O, CO<sub>2</sub>, ions, and urea molecules) along the *z*-axis direction in the H<sub>3%</sub>Urea system for 1.95–2.0 μs. Evolution of (b) the ratio (near the Illite/total number) and (c) the number of h-bonds between the Illite surface and urea/H<sub>2</sub>O. Evolution of (d) the ratio (near the urea/total number), and (e) the average residence time for H<sub>2</sub>O, ions, and CO<sub>2</sub> near urea molecules in the H<sub>3%</sub>Urea system.

decrease, indicating that more H<sub>2</sub>O molecules will form CO<sub>2</sub> hydrates (Figure 2(c) and S6(a–e)). In contrast, the hydrogen bonds between urea molecules and the Illite surface gradually increase (Figure 2(c) and S7(a–e)). At 2.0 μs of the growth simulation, most of the urea is distributed in the Illite interface region (Figure S8(a–e)).

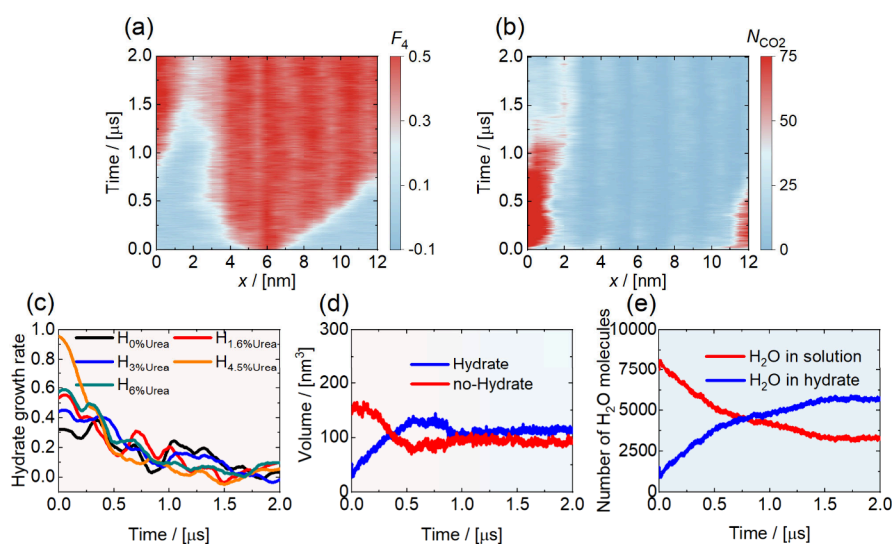
The interactions between urea molecules and surrounding ions/molecules inevitably affect the growth kinetics of the CO<sub>2</sub> hydrate. Urea molecules exhibit varying affinities for geofluids and are beneficial to the growth of CO<sub>2</sub> hydrate growth. CO<sub>2</sub> molecules near the urea gradually decrease as a function of time (Figure 2(d) and S9(a–d)). The residence time of geofluids (H<sub>2</sub>O, CO<sub>2</sub>, and ion) near urea molecules is calculated to characterize the influence of urea molecules on surrounding geofluids. During the 0–0.5 μs of the growth simulation, the value of residence time for CO<sub>2</sub> molecules near urea molecules decreases, indicating that urea molecules

exhibit weak interactions with CO<sub>2</sub> molecules (Figure 2(e) and S10(a–d)). In later stages of the growth simulation (0.5–2.0 μs), the value of residence time for CO<sub>2</sub> molecules near urea molecules increases (Figure 2(e) and S10(a–d)), which is attributed to the growth of CO<sub>2</sub> hydrates to the vicinity of urea molecules. In contrast, the number of H<sub>2</sub>O molecules surrounding the urea molecules gradually decreases (Figure 2(d) and S9(a–d)). A few hydrogen bonds between urea molecules and H<sub>2</sub>O molecules are observed in all systems (Figure S11(a–d) and S12(a–d)). This shows that urea molecules exhibit weak binding to H<sub>2</sub>O molecules. The number of ions surrounding the urea molecules gradually increases (Figure 2(d) and S9(a–d)). The value of the residence time for ions is high and continues to increase (Figure 2(e) and S10(a–d)). These observations indicate that urea molecules exhibit strong binding to ions and weak binding





**Figure 3.** Growth processes of CO<sub>2</sub> hydrate in oceanic sediments for the (a–f) H<sub>3%</sub>Urea system. Illite layers are displayed as polyhedral, i.e., yellow (Si atom), and pink (Al atom). Pink, blue, magenta, orange, and violet represent CO<sub>2</sub>, Cl<sup>−</sup>, Na<sup>+</sup>, K<sup>+</sup>, and urea, respectively. The red circle in (f) highlights the grain boundaries between the CO<sub>2</sub> hydrate crystals. Hydrate cages are shown as sticks in various colors (green for 5<sup>12</sup>6<sup>2</sup>, blue for 5<sup>12</sup>6<sup>3</sup>, red for 5<sup>12</sup>6<sup>4</sup>, orange for 5<sup>12</sup>6<sup>4</sup>, cyan for 4<sup>1</sup>5<sup>10</sup>6<sup>2</sup>, purple for 4<sup>1</sup>5<sup>10</sup>6<sup>3</sup> and pink for 4<sup>1</sup>5<sup>10</sup>6<sup>4</sup>).



**Figure 4.** Evolution of (a) the  $F_4$  order parameters and (b) the number of CO<sub>2</sub> in the nanobubbles ( $N_{\text{CO}_2}$ ) along the  $x$ -axis direction. Evolution of (c) the CO<sub>2</sub> hydrate growth rate ( $R_{\text{HG}}$ ), (d) the volume of CO<sub>2</sub> hydrate crystals, and (e) the number of H<sub>2</sub>O molecules in the CO<sub>2</sub> hydrate and solution in the H<sub>3%</sub>Urea system.

to H<sub>2</sub>O and CO<sub>2</sub> molecules, which is beneficial to CO<sub>2</sub> hydrate growth.

**3.2. Growth Kinetics of CO<sub>2</sub> Hydrates in Oceanic Sediments.** The results revealed that the growth of CO<sub>2</sub> hydrates in oceanic sediments is affected by the confined space, clay surface properties, and presence of organic matter. During the 0–1.0 μs of the growth simulation, the CO<sub>2</sub> hydrate exhibits rapid growth primarily in the  $xy$  direction (Figures 3(a–c), 4(a), S13(a–e), and Video S1). The interfacial H<sub>2</sub>O layer and ion layer on the Illite surface hinder the growth of CO<sub>2</sub> hydrate crystals toward the Illite surface, i.e., the confined space restricts CO<sub>2</sub> hydrate growth. In the homogeneous solution, the CO<sub>2</sub> molecules in the solution form large CO<sub>2</sub> nanobubbles far away from the CO<sub>2</sub> hydrate crystal (Figure 4(b) and S14(a–e)). As the simulation progresses, the CO<sub>2</sub> nanobubbles become small, and a lot of CO<sub>2</sub> molecules detach from the nanobubbles to form CO<sub>2</sub> hydrates (Figures 3(d–f) and S15(a–e)). CO<sub>2</sub> hydrate crystals gradually grow and then occupy the entire Illite nanopores (Figure S16(a–e)). The CO<sub>2</sub> hydrate growth rate ( $R_{\text{HG}}$ ), the volume of the hydrate, and the number of H<sub>2</sub>O molecules in the CO<sub>2</sub> hydrate crystal are shown in Figure 4(c–e), S17(a–e), and S18(a–e). It is

observed that there are two stages during CO<sub>2</sub> hydrate growth, i.e., a rapid growth stage (0–1.0 μs) and a slow growth stage (1.0–2.0 μs). During the 0–1.0 μs of the growth simulation, although the value of  $R_{\text{HG}}$  is declining, it maintains a relatively high  $R_{\text{HG}} > 0.1$  (Figure 4(c)). The volume of the CO<sub>2</sub> hydrates and the number of H<sub>2</sub>O molecules in the CO<sub>2</sub> hydrate crystal also increase rapidly (Figures 4(d–e), S17(a–e), and S18(a–e)). Subsequently (1.0–2.0 μs), the hydrate growth rate ( $R_{\text{HG}}$ ) of the five systems decreases to near-zero levels (Figure 4(c)). The  $R_{\text{HG}}$  is even less than 0, indicating that some CO<sub>2</sub> hydrate dissociates in the later stages of the simulation (Figure 4(c)). The volume of the CO<sub>2</sub> hydrate and the number of H<sub>2</sub>O molecules in the CO<sub>2</sub> hydrate crystal slowly increase (Figure 4(d–e), S17(a–e), and S18(a–e)). During the slow growth stage, the CO<sub>2</sub> hydrate solids occupy the middle region of the Illite nanopores. Two regions are not yet completely occupied, and the occupation rate is very slow, i.e., the crystal contact region and the Illite interface region. Grain boundaries will form between CO<sub>2</sub> hydrate crystals as shown in the red circle in Figure 3(f). The formation of grain boundaries is slower than that of the hydrate crystal growth. At the 2.0 μs of the growth simulation, the grain boundary region is also not fully



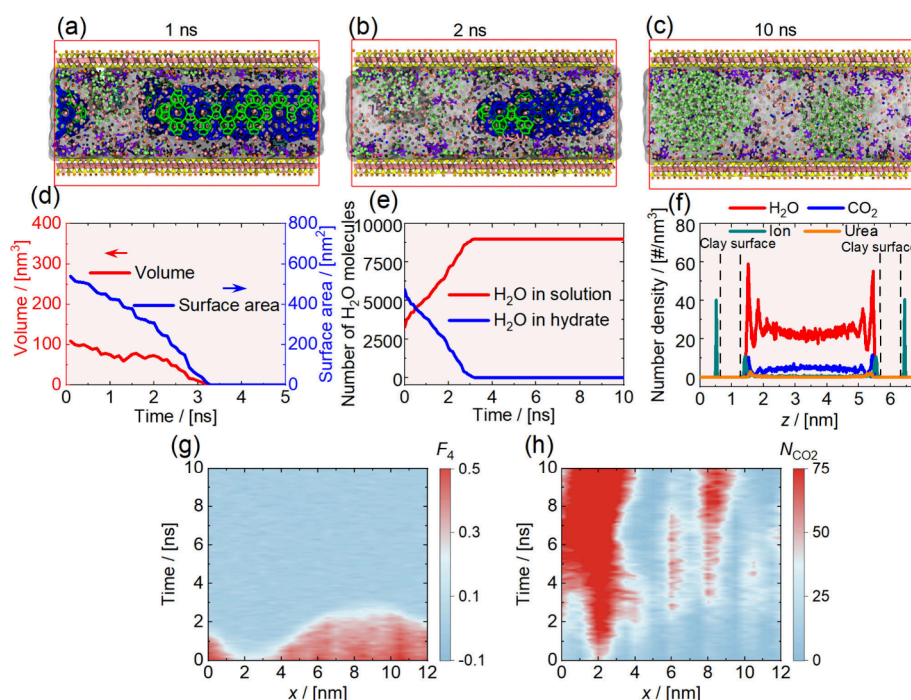


**Figure 5.** Dissociation processes of CO<sub>2</sub> hydrates in (a–c) the H<sub>3%</sub>Urea system. Green and pink balls represent CO<sub>2</sub> molecules in the nanobubble and in solution, respectively. Evolution of (d) volume/surface area of CO<sub>2</sub> hydrate solid, and (e) the number of H<sub>2</sub>O molecules in hydrate and solution. (f) Density distribution curves of H<sub>2</sub>O, CO<sub>2</sub>, ions, and urea molecules along the *z*-axis direction in the H<sub>3%</sub>Urea system over the 9–10 ns. Evolution of (g) the  $F_4$  order parameter and (h) the number of CO<sub>2</sub> in the nanobubbles ( $N_{\text{CO}_2}$ ) along the *x*-axis direction in the H<sub>3%</sub>Urea system.

occupied and contains a large number of nonstandard SI-type hydrate cages (Figure S16(a–e) and S19(a–e)). The growth of the CO<sub>2</sub> hydrate to the Illite interface region is also slow due to the presence of geofluids and surface properties of the Illite.

The  $F_4$  order parameters serve as an effective discriminator for distinguishing the water phase. The values of  $R_{\text{HG}}$  and  $F_4$  in the system without urea molecules are the lowest (Figure 4(c) and S20), indicating that urea molecules can serve as kinetic promoters for the growth of CO<sub>2</sub> hydrate in the Illite nanopores. Previous MD studies have revealed that the higher concentration of guest molecules in water and the lower ion concentration, the more conducive to hydrate formation.<sup>39</sup> Most of the urea molecules are dispersed in the Illite interface region, binding the salt ions and increasing the concentration of CO<sub>2</sub> molecules in the water, thus kinetically promoting CO<sub>2</sub> hydrate growth (Figure S21(a–c)). These findings suggest strategies for incorporating urea into marine sediments and identifying urea-rich marine sediment regions to optimize hydrate-based CO<sub>2</sub> sequestration.

**3.3. The Dissociation of CO<sub>2</sub> Hydrates in Oceanic Sediments.** The dissociation of CO<sub>2</sub> hydrates in oceanic sediments is affected by the surface properties of the Illite and the crystal structure of the CO<sub>2</sub> hydrates. The dissociation processes of CO<sub>2</sub> hydrate in Illite nanopores are shown in Figure 5(a–c) and Video S2. During the 0–1 ns of the dissociation simulation, CO<sub>2</sub> molecules form a small nanobubble and adhere to the Illite surface (Figure 5(a)). During the period of 0–3 ns, both the volume and surface area of CO<sub>2</sub> hydrate decrease sharply (Figure 5(d) and S22(a–e)). Numerous H<sub>2</sub>O molecules transform from the hydrate state to the liquid state (Figure 5(e) and S23(a–e)). Meanwhile, CO<sub>2</sub> nanobubbles adsorbed on the Illite surface become large (Figure 5(b, c, and h)). The dissociation of CO<sub>2</sub> hydrates starts from the regions where hydrate particles are minimally in

contact and extends on both sides (*xy* direction) (Figure 5(g) and S24(a–e)). These interparticle contact zones likely exhibit weaker stability due to incomplete crystal lattice connections, leading to preferential dissociation in these areas. As the simulation processes, several small CO<sub>2</sub> nanobubbles form in regions far away from the large CO<sub>2</sub> nanobubbles (Figure 5(a–b)). This is explained by the fact that the CO<sub>2</sub> molecules produced by the CO<sub>2</sub> hydrate dissociation are far away from the large CO<sub>2</sub> nanobubbles. These CO<sub>2</sub> molecules cannot diffuse into the large nanobubbles immediately, but instead spontaneously form several small nanobubbles. Subsequently, these small nanobubbles will also gradually merge (Figure 5(h) and S25(a–e)). At 10 ns of the dissociation simulation, the CO<sub>2</sub> hydrates have completely dissociated in the five systems (Figure S26 and S27(a–e)). Most of the CO<sub>2</sub> molecules are distributed in spherical CO<sub>2</sub> nanobubbles rather than being dissolved in water (Figure S28(a–c) and S29(a–e)).

During the dissociation of CO<sub>2</sub> hydrate, the Illite surface also exhibits different affinities toward geofluids (H<sub>2</sub>O, CO<sub>2</sub>, ions, and urea molecules) (Figure 5(f)). At 10 ns of the dissociation simulation, large spherical CO<sub>2</sub> nanobubbles are observed in the Illite nanopores and can contact the Illite surfaces (Figure 5(c) and S30(a–d)). CO<sub>2</sub> molecules form the interfacial layer on the Illite surfaces (Figure 5(f), S31(a–e), and S32(a–e)). The majority of ions and urea molecules also accumulate in the Illite interface region rather than diffusing to the center region of the Illite nanopores (Figure S33(a–e) and S34(a–e)). Ions and urea molecules can also form an interfacial layer at the Illite surfaces (Figure 5(f) and S32(a–e)). The distribution of H<sub>2</sub>O molecules during CO<sub>2</sub> hydrate dissociation is consistent with that during CO<sub>2</sub> hydrate growth (Figure S5(a–e) and S35(a–e)).

**3.4. Mechanical Instability of CO<sub>2</sub> Hydrate-Illite Interface in Oceanic Sediments.** The mechanical tension

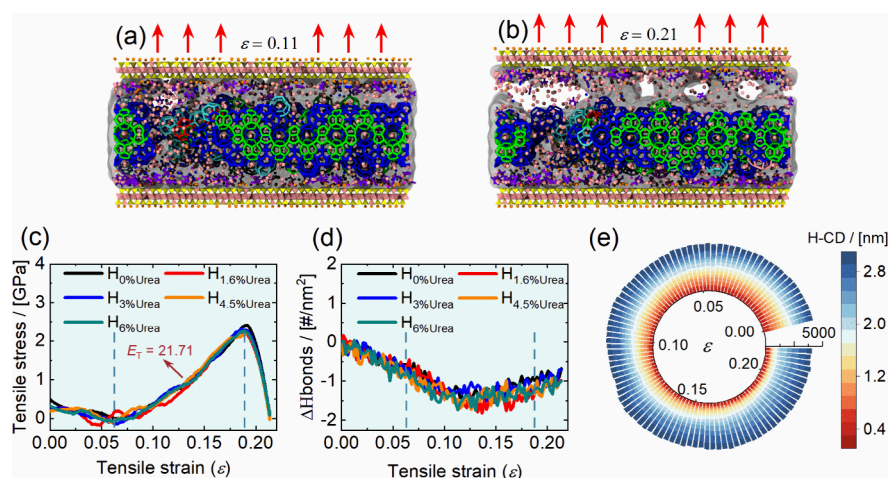


**Figure 6.** Tension snapshots of the CO<sub>2</sub> hydrate-Illite interface in (a–b) the H<sub>3%</sub>Urea system. (c) Mechanical tensile stress–strain curves of the CO<sub>2</sub> hydrate-Illite interface. (d) Increments of the number of hydrogen bonds per square nanometer ( $\Delta$ H bonds) as a function of mechanical tensile strains ( $\epsilon$ ). (e) Number of hydrogen bonds at different distances from the upper Illite surface in the H<sub>3%</sub>Urea system under tensile strain. The  $\Delta$ H bonds are the number of hydrogen bonds between urea/H<sub>2</sub>O molecules and the upper Illite surface.

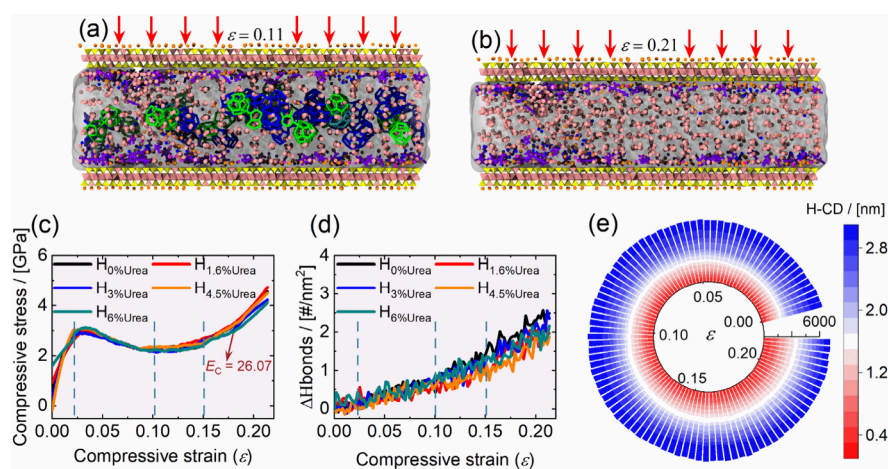


**Figure 7.** Compression snapshots of CO<sub>2</sub> hydrate-Illite interface in (a–b) the H<sub>3%</sub>Urea system. (c) Mechanical compressive stress–strain curves of CO<sub>2</sub> hydrate-Illite interface. (d) Increments of the number of hydrogen bonds ( $\Delta$ H bonds) per square nanometer as a function of mechanical compressive strains ( $\epsilon$ ). (e) Number of hydrogen bonds at different distances from the upper Illite surface in the H<sub>3%</sub>Urea system under compressive strain.

of the CO<sub>2</sub> hydrate-Illite interface exhibits nonlinear characteristics by changing the hydrogen bonds. The tension snapshots of the CO<sub>2</sub> hydrate-Illite interface are shown in Figure 6(a–b). During the tensile deformation processes, the upper Illite surface is gradually stretched (Video S3). The CO<sub>2</sub> hydrate crystals adhere to the lower Illite surface and are separated from the upper Illite interface (Figure 6(a–b) and S36(a–h)). The total number of CO<sub>2</sub> hydrate cages decreases slightly in all of the tension systems (Figure S37(a)). Three tensile deformation stages can be distinguished from the mechanical tensile stress–strain curves (Figure 6(c)). The first tensile deformation stage ( $\epsilon = 0–0.06$ ) is the decrease of tensile stress. The increments of the number of hydrogen bonds per square nanometer ( $\Delta$ H bonds) gradually decrease, attributable to the mechanical tensile stress impeding the formation of hydrogen bonds on the Illite surface (Figure 6(d) and S38(a)). The number of hydrogen bonds at different distances from the upper Illite surface exhibits a small variation (Figure 6(e) and S39(a–e)), indicating that there is little effect on the CO<sub>2</sub> hydrate-Illite interface during this tensile deformation stage.

This observation may be attributed to temperature fluctuations, where an increase from 250 to 273.15 K, potentially affects the stability of geofluids and CO<sub>2</sub> hydrate crystals in the Illite nanopores.

The second tensile deformation stage ( $\epsilon = 0.06–0.18$ ) is characterized as the linear elastic response (Figure 6(c)). The value of the  $\Delta$ H bond on the upper Illite surface decreases (Figure 6(d)). The number of hydrogen bonds within 1.0 nm of the upper Illite surface also decreased drastically (Figure 6(e) and S39(a–e)). These observations indicate that mechanical tensile stress greatly disrupts hydrogen bonds at the CO<sub>2</sub> hydrate-Illite interface. The tensile Young's modulus is approximately 21.71 GPa, which is slightly larger than the value reported by Cao et al.<sup>60</sup> (16.0 GPa) for the CH<sub>4</sub> hydrate-montmorillonite interface. This may be attributed to the presence of urea and salt ions increasing the number of hydrogen bonds on the Illite surface, thereby strengthening the stability of the CO<sub>2</sub> hydrate-Illite interface. As the tensile stress approaches its maximum value, a gradual decrease in the slope of the curves shows strain-softening behavior (Figure 6(c)).



The third tensile deformation stage ( $\epsilon = 0.18\text{--}0.21$ ) is characterized as the brittle fracture behavior (Figure 6(c)). The tensile stress drops sharply from the maximum value to 0 (Figure 6(c)). There is also no change in the number of hydrogen bonds at the distance from the upper Illite surface (Figure 6(e) and S39(a–e)). The CO<sub>2</sub> hydrate is completely separated from the upper Illite interface. It is worth noting that when  $\epsilon = 0.13$ , the  $\Delta H$  bonds value gradually increases (Figure 6(d)), indicating that more H<sub>2</sub>O or urea molecules form hydrogen bonds with the upper Illite surface (Figure S38(a)). This phenomenon may be attributed to the formation of a vacuum area at the CO<sub>2</sub> hydrate-Illite interface (Figure 6(b) and Video S3), which prevents the diffusion of H<sub>2</sub>O and urea molecules near the upper Illite interface toward the CO<sub>2</sub> hydrate crystal and instead stays on the upper Illite surface.

The mechanical compression of the CO<sub>2</sub> hydrate-Illite interface also exhibits nonlinear characteristics by changing the hydrogen bonds and the CO<sub>2</sub> hydrate structure. Snapshots of the compression and mechanical compressive stress–strain curve of the CO<sub>2</sub> hydrate-Illite interface are shown in Figure 7(a–c). During the compressive deformation processes, the upper Illite surface moves toward the lower Illite surface (Video S4), resulting in the gradual disappearance of CO<sub>2</sub> hydrate (Figure 7(a–b) and S40(a–h)). Four compressive deformation stages can be distinguished from the mechanical compressive stress–strain curve (Figure 7(c)). The first compressive deformation stage ( $\epsilon = 0\text{--}0.02$ ) is the increase of compressive stress (Figure 7(c)). In this compressive deformation stage, small changes in the  $\Delta H$  bonds and the number of hydrogen bonds at different distances from the upper Illite surface are observed (Figure 7(d–e), S38(b), and S41(a–e)), indicating that the initial compressive stress exhibits little effect on the hydrogen bonds in the Illite nanopores. This deformation may also be influenced by temperature variations. The second compressive deformation stage ( $\epsilon = 0.02\text{--}0.10$ ) is the decrease of compressive stress (Figure 7(c)). In this compressive deformation stage, the CO<sub>2</sub> hydrate crystal in the middle region of the Illite nanopores dissociates (Figure S37(b)). Although the  $\Delta H$  bonds value increases, the number of hydrogen bonds at different distances from the upper Illite surface exhibits little change (Figure 7(d–e), S38(b), and S41(a–e)). The presence of the CO<sub>2</sub> hydrate cage creates a large hydrogen bond network, which alleviates compressive stress.

The third compressive deformation stage ( $\epsilon = 0.10\text{--}0.15$ ) is characterized as the strain-hardening behavior. In this compressive deformation stage, the compressive stress increases, and the slope of the curves increases slowly (Figure 7(c)). This is attributed to the fact that the number of residual CO<sub>2</sub> hydrate cages gradually decreases until complete disappearance (Figure S37(b)). These residual hydrate cages are unable to alleviate compressive stress. The fourth compressive deformation stage ( $\epsilon = 0.15\text{--}0.21$ ) is characterized as the linear elastic response (Figure 7(c)). The value of  $\Delta H$  bonds and the number of hydrogen bonds within 1.0 nm from the upper surface increase (Figures 7(d–e), S38(b), and S41(a–e)). In this compressive deformation stage, the CO<sub>2</sub> hydrate crystals completely dissociated. The compressive Young's modulus is approximately 26.07 GPa, which is also slightly larger than the value reported by Cao et al.<sup>60</sup> (20.0 GPa) for the CH<sub>4</sub> hydrate-montmorillonite interface. This difference may be related to the presence of CO<sub>2</sub> hydrate crystals. At this stage of the study, the standard CO<sub>2</sub> hydrate

cages have completely disappeared, leaving only the hydrogen bonding network.

#### 4. CONCLUSIONS

Systematic molecular dynamics simulations are executed to investigate the growth and dissociation of CO<sub>2</sub> hydrates, and the mechanical instability of the CO<sub>2</sub> hydrate-Illite interface in the brine-urea-Illite system. The simulations reveal that the growth of the CO<sub>2</sub> hydrate in oceanic sediments is affected by the confined space, clay surface properties, and presence of urea. Specifically, the interfacial H<sub>2</sub>O and ion layers on the Illite surface hinder the growth of CO<sub>2</sub> hydrate crystals toward the Illite surfaces. Urea molecules are dispersed in the Illite interface region, binding the salt ions and increasing the concentration of CO<sub>2</sub> molecules in the water, thus kinetically promoting CO<sub>2</sub> hydrate growth. The dissociation of CO<sub>2</sub> hydrates in oceanic sediments is affected by the Illite surface properties and the crystal structure of the CO<sub>2</sub> hydrates. CO<sub>2</sub> hydrate dissociation starts from the regions where hydrate particles are minimally in contact and extends on both sides. Then, large spherical CO<sub>2</sub> nanobubbles are formed that can contact the Illite surfaces. The mechanical tension of the CO<sub>2</sub> hydrate-Illite interface exhibits nonlinear characteristics by changing the hydrogen bonds on the Illite surfaces and in the Illite nanopores. There are three tensile deformation stages at the CO<sub>2</sub> hydrate-Illite interface at tensile strains, i.e., (1) the decrease of tensile stress, (2) the linear elastic response, and (3) the brittle fracture behavior. The mechanical compression of the CO<sub>2</sub> hydrate-Illite interface also exhibits nonlinear characteristics by changing the hydrogen bonds and the CO<sub>2</sub> hydrate structure. There are four compressive deformation stages at the CO<sub>2</sub> hydrate-Illite interface at compressive strains, i.e., (1) the increase of compressive stress, (2) the decrease of compressive stress, (3) the strain-hardening behavior, and (4) the linear elastic response. The molecular insight into the growth and dissociation of CO<sub>2</sub> hydrates, and the mechanical instability of CO<sub>2</sub> hydrate-Illite interface in oceanic sediments contributes to a broader understanding of hydrate-based CO<sub>2</sub> sequestration. We feel that this preliminary investigation is poised to catalyze further original research, particularly in uncovering novel CO<sub>2</sub> hydrate promoters and identifying potential marine CO<sub>2</sub> sequestration sites.

#### ■ ASSOCIATED CONTENT

##### Supporting Information

The Supporting Information is available free of charge at <https://pubs.acs.org/doi/10.1021/acs.jpcc.4c05413>.

Video S1: Growth process of CO<sub>2</sub> hydrate in oceanic sediments for the H<sub>3%</sub>Urea growth system (AVI)

Video S2: Dissociation process of CO<sub>2</sub> hydrate in oceanic sediments for the H<sub>3%</sub>Urea dissociation system (AVI)

Video S3: Tension process of the CO<sub>2</sub> hydrate-Illite interface in oceanic sediments for the H<sub>3%</sub>Urea instability system (AVI)

Video S4: Compression process of the CO<sub>2</sub> hydrate-Illite interface in oceanic sediments for the H<sub>3%</sub>Urea instability system (AVI)

Parameters and force field for the systems; additional details of the simulation models and methods; calculation principles; number densities of CO<sub>2</sub>, H<sub>2</sub>O, ions, and urea; number of molecules near clay and urea;



hydrogen bonds; average residence time;  $F_4$ ; number of  $\text{CO}_2$  in the nanobubbles;  $\text{CO}_2$  mole fraction in water, growth snapshots of  $\text{CO}_2$  hydrates; volume of  $\text{CO}_2$  hydrate solids; number of  $\text{H}_2\text{O}$  molecules in hydrate and solution; dissociation snapshots of  $\text{CO}_2$  hydrates; tensile and compressive snapshots of  $\text{CO}_2$  hydrate-illite interface; number of  $\text{CO}_2$  hydrate cages under tensile and compressive strains; number of hydrogen bonds at different distances from the upper illite surface under tensile and compressive (PDF)

## AUTHOR INFORMATION

### Corresponding Authors

**Fulong Ning** – National Center for International Research on Deep Earth Drilling and Resource Development, Faculty of Engineering, China University of Geosciences, Wuhan, Hubei 430074, China; [orcid.org/0000-0003-1236-586X](https://orcid.org/0000-0003-1236-586X); Email: [nflzx@cug.edu.cn](mailto:nflzx@cug.edu.cn)

**Thijs J.H. Vlugt** – Engineering Thermodynamics, Process & Energy Department, Faculty of Mechanical Engineering, Delft University of Technology, Delft 2628CB, The Netherlands; [orcid.org/0000-0003-3059-8712](https://orcid.org/0000-0003-3059-8712); Email: [t.j.h.vlugt@tudelft.nl](mailto:t.j.h.vlugt@tudelft.nl)

### Authors

**Fengyi Mi** – National Center for International Research on Deep Earth Drilling and Resource Development, Faculty of Engineering, China University of Geosciences, Wuhan, Hubei 430074, China; Engineering Thermodynamics, Process & Energy Department, Faculty of Mechanical Engineering, Delft University of Technology, Delft 2628CB, The Netherlands; [orcid.org/0000-0002-1537-0683](https://orcid.org/0000-0002-1537-0683)

**Wei Li** – National Center for International Research on Deep Earth Drilling and Resource Development, Faculty of Engineering, China University of Geosciences, Wuhan, Hubei 430074, China

**Jiangtao Pang** – National Center for International Research on Deep Earth Drilling and Resource Development, Faculty of Engineering, China University of Geosciences, Wuhan, Hubei 430074, China; [orcid.org/0000-0002-1882-9920](https://orcid.org/0000-0002-1882-9920)

**Othonas A. Moulτος** – Engineering Thermodynamics, Process & Energy Department, Faculty of Mechanical Engineering, Delft University of Technology, Delft 2628CB, The Netherlands; [orcid.org/0000-0001-7477-9684](https://orcid.org/0000-0001-7477-9684)

Complete contact information is available at:

<https://pubs.acs.org/10.1021/acs.jpcc.4c05413>

### Notes

The authors declare no competing financial interest.

## ACKNOWLEDGMENTS

This work was supported by the National Science Foundation for Distinguished Young Scholars (42225207), the National Natural Science Foundation of China (52104045), the Natural Science Foundation of Hubei Province (2021CFA024), and the China Scholarship Council (CSC202306410133). The authors acknowledge the use of computational resources of the DelftBlue supercomputer, provided by the Delft High Performance Computing Centre (<https://www.tudelft.nl/dhpc>).

## REFERENCES

- (1) Liu, F.-P.; Li, A.-R.; Qing, S.-L.; Luo, Z.-D.; Ma, Y.-L. Formation kinetics, mechanism of  $\text{CO}_2$  hydrate and its applications. *Renewable Sustainable Energy Rev.* **2022**, *159*, 112221.
- (2) Sinehbaghizadeh, S.; Saptoro, A.; Mohammadi, A. H.  $\text{CO}_2$  hydrate properties and applications: A state of the art. *Prog. Energy Combust. Sci.* **2022**, *93*, 101026.
- (3) Ma, Z. W.; Zhang, P.; Bao, H. S.; Deng, S. Review of fundamental properties of  $\text{CO}_2$  hydrates and  $\text{CO}_2$  capture and separation using hydration method. *Renewable Sustainable Energy Rev.* **2016**, *53*, 1273–1302.
- (4) Sloan, E. D.; Koh, C. A. *Clathrate Hydrates of Natural Gases*; 3rd ed., CRC Press: Boca Raton, FL, 2008.
- (5) Brewer, P. G.; Friederich, G.; Peltzer, E. T.; Orr, F. M., Jr Direct experiments on the ocean disposal of fossil fuel  $\text{CO}_2$ . *Science* **1999**, *284*, 943–945.
- (6) Ning, F. L.; Yu, Y. B.; Kjelstrup, S.; Vlugt, T. J. H.; Glavatskiy, K. Mechanical properties of clathrate hydrates: status and perspectives. *Energy Environ. Sci.* **2012**, *5*, 6779–6795.
- (7) Zhang, Z.; Liu, L. L.; Lu, W. J.; Liu, C. L.; Ning, F. L.; Dai, S. Permeability of hydrate-bearing fine-grained sediments: Research status, challenges and perspectives. *Earth Sci. Rev.* **2023**, *244*, 104517.
- (8) Mi, F.; He, Z.; Jiang, G.; Ning, F. Effect of Glucose on  $\text{CH}_4$  Hydrate Formation in Clay Nanopores and Bulk Solution: Insights from Microsecond Molecular Dynamics Simulations. *ACS Sustain. Chem. Eng.* **2024**, *12*, 4644–4654.
- (9) Zhao, J.; Liu, Y.; Yang, L.; Zhang, L.; Song, Y. Organics-Coated Nanoclays Further Promote Hydrate Formation Kinetics. *J. Phys. Chem. Lett.* **2021**, *12*, 3464–3467.
- (10) Ye, J.-l.; Qin, X.-w.; Xie, W.-w.; Lu, H.-l.; Ma, B.-j.; Qiu, H.-j.; Liang, J.-q.; Lu, J.-a.; Kuang, Z.-g.; Lu, C.; et al. The second natural gas hydrate production test in the South China Sea. *China Geology* **2020**, *3*, 197–209.
- (11) Guggenheim, S.; Koster van Groos, A. F. New gas-hydrate phase: Synthesis and stability of clay-methane hydrate intercalate. *Geology* **2003**, *31*, 653–656.
- (12) Kim, D.; Ahn, Y.-H.; Kim, S.-J.; Lee, J. Y.; Lee, J.; Seo, Y.-j.; Lee, H. Gas Hydrate in Crystalline-Swelled Clay: The Effect of Pore Dimension on Hydrate Formation and Phase Equilibria. *J. Phys. Chem. C* **2015**, *119*, 22148–22153.
- (13) Uchida, T.; Takeya, S.; Chuvilin, E. M.; Ohmura, R.; Nagao, J.; Yakushev, V. S.; Istomin, V. A.; Minagawa, H.; Ebinuma, T.; Narita, H. Decomposition of methane hydrates in sand, sandstone, clays, and glass beads. *Journal of Geophysical Research: Solid Earth* **2004**, *109*(B5), DOI: 10.1029/2003JB002771.
- (14) Li, Y.; Liu, L.; Jin, Y.; Wu, N. Characterization and development of natural gas hydrate in marine clayey-silt reservoirs: A review and discussion. *Advances in Geo-Energy Research* **2021**, *5*, 75–86.
- (15) Wu, Z.; Li, Y.; Sun, X.; Wu, P.; Zheng, J. Experimental study on the effect of methane hydrate decomposition on gas phase permeability of clayey sediments. *Appl. Energy* **2018**, *230*, 1304–1310.
- (16) Wu, C.; Fan, S.; Wang, Y.; Lang, X.; Li, G. Experiment and observation of methane hydrate formation in silty clay sediments of the South China sea with 50–85% water saturation. *Energ Fuels* **2022**, *36*, 10529–10540.
- (17) Liu, Z.; Zheng, J. J.; Wang, Z. Y.; Gao, Y. H.; Sun, B. J.; Liao, Y. Q.; Linga, P. Effect of clay on methane hydrate formation and dissociation in sediment: Implications for energy recovery from clayey-sandy hydrate reservoirs\*. *Appl. Energy* **2023**, *341*, 121064.
- (18) Sun, Y.; Jiang, S.; Li, S.; Wang, X.; Peng, S. Hydrate formation from clay bound water for  $\text{CO}_2$  storage. *Chem. Eng. J.* **2021**, *406*, 126872.
- (19) Bello-Palacios, A.; Almenningen, S.; Fotland, P.; Ersland, G. Experimental and Numerical Analysis of the Effects of Clay Content on  $\text{CH}_4$  Hydrate Formation in Sand. *Energ Fuels* **2021**, *35*, 9836–9846.
- (20) Feng, Y.; Qu, A.; Han, Y.; Shi, C.; Liu, Y.; Zhang, L.; Zhao, J.; Yang, L.; Song, Y. Effect of gas hydrate formation and dissociation on

- porous media structure with clay particles. *Appl. Energy* **2023**, *349*, 121694.
- (21) Park, T.; Kwon, T. H. Effect of Electric Field on Gas Hydrate Nucleation Kinetics: Evidence for the Enhanced Kinetics of Hydrate Nucleation by Negatively Charged Clay Surfaces. *Environ. Sci. Technol.* **2018**, *52*, 3267–3274.
- (22) Cha, S. B.; Ouar, H.; Wildeman, T. R.; Sloan, E. D. A third-surface effect on hydrate formation. *J. Phys. Chem.* **1988**, *92*, 6492–6494.
- (23) Ren, J. J.; Liu, X. H.; Niu, M. Y.; Yin, Z. Y. Effect of sodium montmorillonite clay on the kinetics of CH<sub>4</sub> hydrate-implication for energy recovery. *Chem. Eng. J.* **2022**, *437*, 135368.
- (24) Ren, J. J.; Zeng, S. Y.; Chen, D. Y.; Yang, M. J.; Linga, P.; Yin, Z. Y. Roles of montmorillonite clay on the kinetics and morphology of CO<sub>2</sub> hydrate in hydrate-based CO<sub>2</sub> sequestration. *Appl. Energy* **2023**, *340*, 120997.
- (25) Ren, J.; Yin, Z.; Li, Q.; Wu, F.; Chen, D.; Li, S. Pore-scale investigation of CH<sub>4</sub> hydrate kinetics in clayey-silty sediments by Low-Field NMR. *Energ Fuels* **2022**, *36*, 14874–14887.
- (26) Mi, F.; He, Z.; Jiang, G.; Ning, F. Effects of marine environments on methane hydrate formation in clay nanopores: A molecular dynamics study. *Sci. Total Environ.* **2022**, *852*, 158454.
- (27) Asadi, F.; Ejtemaei, M.; Birkett, G.; Searles, D. J.; Nguyen, A. V. The link between the kinetics of gas hydrate formation and surface ion distribution in the low salt concentration regime. *Fuel* **2019**, *240*, 309–316.
- (28) Choudhary, N.; Kushwaha, O. S.; Bhattacharjee, G.; Chakrabarty, S.; Kumar, R. Macro and Molecular Level Insights on Gas Hydrate Growth in the Presence of Hofmeister Salts. *Ind. Eng. Chem. Res.* **2020**, *59*, 20591–20600.
- (29) Nguyen, N. N.; Nguyen, A. V. The dual effect of sodium halides on the formation of methane gas hydrate. *Fuel* **2015**, *156*, 87–95.
- (30) Farhang, F.; Nguyen, A. V.; Hampton, M. A. Influence of Sodium Halides on the Kinetics of CO<sub>2</sub> Hydrate Formation. *Energ Fuels* **2014**, *28*, 1220–1229.
- (31) Walsh, M. R.; Koh, C. A.; Sloan, E. D.; Sum, A. K.; Wu, D. T. Microsecond simulations of spontaneous methane hydrate nucleation and growth. *Science* **2009**, *326*, 1095–1098.
- (32) Zhang, Z.; Kusalik, P. G.; Liu, C.; Wu, N. Methane hydrate formation in slit-shaped pores: Impacts of surface hydrophilicity. *Energy* **2023**, *285*, 129414.
- (33) Chen, Y.; Takeya, S.; Sum, A. K. Topological dual and extended relations between networks of clathrate hydrates and Frank-Kasper phases. *Nat. Commun.* **2023**, *14*, 596.
- (34) Li, Y.; Chen, M.; Tang, H.; Han, S. B.; Song, H. Z.; Wang, P. F.; Zhao, Y. S.; Zhu, J. L. Insights into Carbon Dioxide Hydrate Nucleation on the External Basal Surface of Clay Minerals from Molecular Dynamics Simulations. *ACS Sustain. Chem. Eng.* **2022**, *10*, 6358–6369.
- (35) Liao, B.; Wang, J.; Han, X.; Wang, R.; Lv, K.; Bai, Y.; Jiang, H.; Shao, Z.; Wang, Y.; Sun, J. Microscopic molecular insights into clathrate methane hydrates dissociation in a flowing system. *Chem. Eng. J.* **2022**, *430*, 133098.
- (36) Li, W.; Pang, J.; Peng, L.; Fang, B.; Ou, W.; Tao, Z.; Liu, Z.; Ning, F. Microscopic Insights into the Effects of Anti-Agglomerant Surfactants on Surface Characteristics of Tetrahydrofuran Hydrate. *Energ Fuels* **2023**, *37*, 3741–3751.
- (37) Wang, R.; Liao, B.; Wang, J.; Sun, J.; Wang, Y.; Wang, J.; Wang, Q.; Qu, Y.; Cheng, R. Microscopic molecular insights into methane hydrate growth on the surfaces of clay minerals: Experiments and molecular dynamics simulations. *Chem. Eng. J.* **2023**, *451*, 138757.
- (38) He, Z.; Mi, F.; Ning, F. Molecular insights into CO<sub>2</sub> hydrate formation in the presence of hydrophilic and hydrophobic solid surfaces. *Energy* **2021**, *234*, 121260.
- (39) Mi, F.; He, Z.; Zhao, Y.; Jiang, G.; Ning, F. Effects of surface property of mixed clays on methane hydrate formation in nanopores: A molecular dynamics study. *J. Colloid Interface Sci.* **2022**, *627*, 681–691.
- (40) He, Z. J.; Mi, F. Y.; Ning, F. L.; Pang, J. T.; Jiang, G. S. Methane Hydrate Formation in the Salty Water Confined in Clay Nanopores: A Molecular Simulation Study. *ACS Sustain. Chem. Eng.* **2022**, *10*, 6128–6140.
- (41) Mi, F.; He, Z.; Cheng, L.; Jiang, G.; Ning, F. Molecular dynamics simulation on methane hydrate formation in clay nanopores of edge surfaces. *Appl. Clay Sci.* **2023**, *243*, 107069.
- (42) Liu, Y.; Zhang, L.; Yang, L.; Dong, H.; Zhao, J.; Song, Y. Behaviors of CO<sub>2</sub> Hydrate Formation in the Presence of Acid-Dissolvable Organic Matters. *Environ. Sci. Technol.* **2021**, *55*, 6206–6213.
- (43) Liu, Y. Z.; Feng, Y.; Zhang, L. X.; Song, Y. C.; Yang, L.; Zhao, J. F. Effects of protein macromolecules and metabolic small molecules on kinetics of methane hydrate formation in marine clay. *Chem. Eng. J.* **2021**, *412*, 128496.
- (44) Park, T.; Kyung, D.; Lee, W. Effect of organic matter on CO<sub>2</sub> hydrate phase equilibrium in phyllosilicate suspensions. *Environ. Sci. Technol.* **2014**, *48*, 6597–6603.
- (45) Yun, S.; Jo, I.; Go, W.; Kim, Y.; Kim, K.-S.; Seo, Y. Water-Soluble Cellulose As a New Class of Green CH<sub>4</sub> Hydrate Inhibitors: Insights from Experiments and Molecular Dynamics Simulations. *ACS Sustain. Chem. Eng.* **2023**, *11*, 6153–6162.
- (46) Jia, Y.; Zhao, Y.; Li, M.; Zhang, L.; Liu, Y.; Dong, H.; Zhao, J.; Yang, L.; Song, Y. Biodegradable Organics as a Multisystem-Compatible Low-Dose Green Kinetic Hydrate Inhibitor. *ACS Sustain. Chem. Eng.* **2022**, *10*, 11320–11329.
- (47) Fengyi, M.; Zhongjin, H.; Guosheng, J.; Fulong, N. Molecular insights into the effects of lignin on methane hydrate formation in clay nanopores. *Energy* **2023**, *276*, 127496.
- (48) Ji, H. Q.; Wu, G. Z.; Zi, M. C.; Chen, D. Y. Microsecond Molecular Dynamics Simulation of Methane Hydrate Formation in Humic-Acid-Amended Sodium Montmorillonite. *Energ Fuels* **2016**, *30*, 7206–7213.
- (49) Ji, H. Q.; Chen, D. Y.; Zhao, C.; Wu, G. Z. Molecular Dynamics Simulation of Methane Hydrate Formation and Dissociation in the Clay Pores with Fatty Acids. *J. Phys. Chem. C* **2018**, *122*, 1318–1325.
- (50) Kyung, D.; Lim, H. K.; Kim, H.; Lee, W. CO<sub>2</sub> hydrate nucleation kinetics enhanced by an organo-mineral complex formed at the montmorillonite-water interface. *Environ. Sci. Technol.* **2015**, *49*, 1197–1205.
- (51) Sowa, B.; Zhang, X. H.; Kozielski, K. A.; Hartley, P. G.; Dunstan, D. E.; Maeda, N. Nucleation probability distributions of methane-propane mixed gas hydrates in salt solutions and urea. *Energ Fuels* **2015**, *29*, 6259–6270.
- (52) Muromachi, S.; Abe, T.; Maekawa, T.; Yamamoto, Y. Phase equilibrium for clathrate hydrate formed in methane+ water+ urea system. *Fluid Phase Equilib.* **2015**, *398*, 1–4.
- (53) Go, W.; Lee, D.; Seo, Y. Synergistic inhibition effects of hydrophilic monomeric substances on CH<sub>4</sub> hydrate as revealed by experimental and computational approaches. *Chem. Eng. J.* **2021**, *426*, 130794.
- (54) Gong, Y.; Mendgaziev, R. I.; Hu, W.; Li, Y.; Li, Z.; Stoporev, A. S.; Manakov, A. Y.; Vinokurov, V. A.; Li, T.; Semenov, A. P. Urea as a green thermodynamic inhibitor of sII gas hydrates. *Chem. Eng. J.* **2022**, *429*, 132386.
- (55) Bavoh, C. B.; Lal, B.; Osei, H.; Sabil, K. M.; Mukhtar, H. A review on the role of amino acids in gas hydrate inhibition, CO<sub>2</sub> capture and sequestration, and natural gas storage. *J. Nat. Gas Sci. Eng.* **2019**, *64*, 52–71.
- (56) Lim, L. H. V.; Lloren, A. V.; Lamorena, R. B. The effect of urea in the nucleation process of CO<sub>2</sub> clathrate hydrates. *J. Mol. Liq.* **2014**, *194*, 245–250.
- (57) Sinehbaghizadeh, S.; Saptoro, A.; Naeiji, P.; Tiong, A. N. T.; Mohammadi, A. H. Insights into the synergistic effects of metal particles (Ag, Cu, and Fe) and urea on CO<sub>2</sub> clathrate hydrate growth using molecular dynamics simulations. *Chem. Eng. Sci.* **2022**, *264*, 118194.

- (58) Wang, P. W.; Wu, D. T.; Lin, S. T. Promotion mechanism for the growth of CO<sub>2</sub> hydrate with urea using molecular dynamics simulations. *Chem. Commun.* **2021**, *57*, 5330–5333.
- (59) Sinehbaghzadeh, S.; Saptorio, A.; Naeiji, P.; Mohammadi, A. H. Molecular dynamics simulations to investigate the effects of organic amines on biogas clathrate hydrate formation. *J. Mol. Liq.* **2023**, *382*, 122015.
- (60) Cao, P.; Li, T.; Ning, F.; Wu, J. Mechanical Instability of Methane Hydrate-Mineral Interface Systems. *ACS Appl. Mater. Interfaces* **2021**, *13*, 46043–46054.
- (61) Wu, J.; Ning, F.; Trinh, T. T.; Kjelstrup, S.; Vlugt, T. J. H.; He, J.; Skallerud, B. H.; Zhang, Z. Mechanical instability of monocrystalline and polycrystalline methane hydrates. *Nat. Commun.* **2015**, *6*, 8743.
- (62) Zhang, Z.; Kusalik, P. G.; Wu, N.; Liu, C.; Zhang, Y. Molecular simulation study on the stability of methane hydrate confined in slit-shaped pores. *Energy* **2022**, *257*, 124738.
- (63) Mi, F.; He, Z.; Ning, F. Molecular insight on CO<sub>2</sub>/C<sub>3</sub>H<sub>8</sub> mixed hydrate formation from the brine for sustainable hydrate-based desalination. *Sep. Purif. Technol.* **2025**, *353*, 128244.
- (64) Mi, F.; He, Z.; Jiang, G.; Ning, F. What roles do interlayer cations (K<sup>+</sup>) and salt ions (Na<sup>+</sup> and Cl<sup>-</sup>) play in methane hydrate formation in Illite nanopore? *Appl. Clay Sci.* **2024**, *256*, 107428.
- (65) Narayanan Nair, A. K.; Cui, R.; Sun, S. Overview of the adsorption and transport properties of water, ions, carbon dioxide, and methane in swelling clays. *ACS Earth Space Chem.* **2021**, *5*, 2599–2611.
- (66) Mi, F. Y.; He, Z. J.; Fang, B.; Ning, F. L.; Jiang, G. S. Molecular insights into the effects of surface property and pore size of non-swelling clay on methane hydrate formation. *Fuel* **2022**, *311*, 122607.
- (67) Fang, B.; Lü, T.; Li, W.; Moulton, O. A.; Vlugt, T. J. H.; Ning, F. Microscopic insights into poly- and mono-crystalline methane hydrate dissociation in Na-montmorillonite pores at static and dynamic fluid conditions. *Energy* **2024**, *288*, 129755.
- (68) Potoff, J. J.; Siepmann, J. I. Vapor-liquid equilibria of mixtures containing alkanes, carbon dioxide, and nitrogen. *AIChE J.* **2001**, *47*, 1676–1682.
- (69) Abascal, J. L.; Sanz, E.; Garcia Fernandez, R.; Vega, C. A potential model for the study of ices and amorphous water: TIP4P/Ice. *J. Chem. Phys.* **2005**, *122*, 234511.
- (70) Cygan, R. T.; Liang, J. J.; Kalinichev, A. G. Molecular models of hydroxide, oxyhydroxide, and clay phases and the development of a general force field. *J. Phys. Chem. B* **2004**, *108*, 1255–1266.
- (71) Jorgensen, W. L.; Maxwell, D. S.; TiradoRives, J. Development and testing of the OPLS all-atom force field on conformational energetics and properties of organic liquids. *J. Am. Chem. Soc.* **1996**, *118*, 11225–11236.
- (72) Abraham, M. J.; Murtola, T.; Schulz, R.; Páll, S.; Smith, J. C.; Hess, B.; Lindahl, E. GROMACS: High performance molecular simulations through multi-level parallelism from laptops to supercomputers. *SoftwareX* **2015**, *1*, 19–25.
- (73) Nosé, S. A Molecular-Dynamics Method for Simulations in the Canonical Ensemble. *Mol. Phys.* **1984**, *52*, 255–268.
- (74) Parrinello, M.; Rahman, A. Crystal-Structure and Pair Potentials - a Molecular-Dynamics Study. *Phys. Rev. Lett.* **1980**, *45*, 1196–1199.
- (75) Darden, T.; York, D.; Pedersen, L. Particle mesh Ewald: An N·log(N) method for Ewald sums in large systems. *J. Chem. Phys.* **1993**, *98*, 10089–10092.